Nickel single-atom catalysts intrinsically promoted by fast pyrolysis for selective electroreduction of CO_2 into CO

Yibo Guo [a], Sai Yao [a], Yuanyuan Xue [a], Xu Hu [a], Huijuan Cui [b],[*], Zhen Zhou [a],[c],[**]

[a] School of Materials Science and Engineering, Institute of New Energy Material Chemistry, Key Laboratory of Advanced Energy Materials Chemistry (Ministry of Education), Renewable Energy Conversion and Storage Center (ReCast), Nankai University, Tianjin 300350, China
[b] Tianjin Institute of Industrial Biotechnology, Chinese Academy of Sciences, 32 West 7th Avenue, Tianjin Airport Economic Area, Tianjin 300308, China
[c] Engineering Research Center of Advanced Functional Material Manufacturing of Ministry of Education, School of Chemical Engineering, Zhengzhou University, Zhengzhou 450001, China

ABSTRACT

The electrochemical reduction reaction of carbon dioxide (CO_2RR) is an effective way towards carbon neutralization. Single-atom catalysts (SACs) are expected to be efficient for CO_2RR due to maximum atom utilization and excellent catalytic performance. Here, nitrogen-doped carbon supported Ni SACs (Ni-SAC@NCs) were prepared through effective fast pyrolysis. CO_2 can convert into CO efficiently with Ni-SAC@NCs as electrocatalysts for CO_2RR. The faradaic efficiency kept well above 80% in the applied potential window of −0.6 to −0.9 V (vs. reversible hydrogen electrode (RHE)), with a highest FE_{CO} of 95% at −0.6 V (vs. RHE). Ni-SAC@NCs can achieve the best CO selectivity under a small overpotential, surpassing most other state-of-the-art catalysts. Computations also indicate that the unique defect-Ni-N_3 structure is the active site. This work not only provides a simple and promising new route for the preparation of SACs, but also proves the key role of the coordination environment in electrocatalysis.

1. Introduction

The electrochemical reduction reaction of CO_2 (CO_2RR) with electricity generated from renewable energy sources is considered to be an effective solution to solve the global excess CO_2 emission and achieve carbon neutralization [1]. However, due to the stable chemical bonding of CO_2 and the competitive hydrogen evolution reaction (HER) in aqueous systems, efficient electrocatalysts are required for CO_2RR [2]. Single-atom catalysts (SACs) have received more attention due to their excellent performance. The SACs have unique electronic properties and can achieve ultra-high selectivity for CO_2RR [3–7]. For example, Pan et al. reported a Co SAC coordinated by five N atoms, with CO selectivity close to 100% and excellent stability, and proved that the unique structure of Co-N_5 is beneficial to the formation of intermediate COOH* and the desorption of CO [8]. Rong et al. reported a Ni-N_3-Vac SAC with three N atoms and a vacancy, which showed extremely high CO_2 reduction current density of 65 mA cm^{-2} and high CO Faradaic efficiency (FE) over 90% at 0.9 V vs. RHE. Density functional theory (DFT)

computations indicate that the presence of a vacancy can greatly promote the electrocatalytic activity for CO_2 reduction [9]. However, there is still some deficiency in the current studies on SACs. First, the preparation of SACs is difficult, especially in the preparation involving high-temperature calcination, which will inevitably lead to metal agglomeration and destroy the coordination environment of single atoms [10–12]. Therefore, it is urgent to develop preparation methods that can intrinsically inhibit metal agglomeration. Moreover, the mechanism of the interaction between metal atoms, coordination atoms and supports should be further explored [13].

On basis of the above consideration, we innovatively adopt an effective strategy of fast pyrolysis to prepare nitrogen doped carbon supported Ni SACs (Ni-SAC@NCs). High temperature can promote the decomposition of precursors, while the instantaneous high internal pressure produced by fast pyrolysis of carbon-containing precursors can intrinsically inhibit the agglomeration of metal atoms to achieve high dispersion of single atoms. Ni-SAC@NCs exhibit excellent CO_2RR performance with a highest FE_{CO} of 95% at −0.6 V (vs. RHE) under H-cell

tests and the CO partial current of 187.7 mA cm^{-2} was obtained at 2.7 V cell voltage under flow cell tests. DFT computations further disclose that the configuration of Ni-SAC@NCs profit the production of the final product CO. All the above results explain the origin of catalytic activity of Ni SACs from a deeper perspective.

2. Experimental

2.1. Materials preparation

Glucose (99.5%), sodium carbonate (99.8%), L-alanine (99.0%) and nickel(II) acetate tetrahydrate (99.9%) (analytical grade, Aladdin) were used as received. Sodium carbonate (12.7 g), glucose (5.4 g), L-alanine (2.67 g) and nickel(II) acetate tetrahydrate (0.075 g) were uniformly mixed and ground in an agate mortar. The mixture was then placed in a tubular furnace equipped with repetitive thermal shock equipment (Fig. S1, Supporting Information) to achieve high temperature rapid pyrolysis. The mixture was heat treated for 90 s at 1000 °C under an argon atmosphere (99.9999%, Air Liquide) and then cooled to room temperature. Sodium carbonate was then removed by water rinse, wherein sodium carbonate was collected by purification and can be reused (Fig. S2). The product was then dried overnight in an oven at 60 °C. Then the sample was annealed at 900 °C under an argon atmosphere for half an hour at a heating rate of 5 °C per minute to increase the graphitization. The obtained sample was named as Ni-SAC@NC.

For synthesis of Ni-SAC@C as a control sample, sodium carbonate (12.7 g), glucose (5.4 g) and nickel(II) acetate tetrahydrate (0.075 g) were uniformly mixed and ground in an agate mortar. The same processing steps as the preparation of Ni-SAC@NC were repeated, and the obtained sample was named as Ni-SAC@C.

For synthesis of other control samples, C, N-C and Ni-N-C, the details can be found the Supporting Information.

2.2. Materials characterization

The morphology and structure of the electrocatalysts were examined by field emission scanning electron microscope (FESEM, JSM-7800F), transmission electron microscope (TEM, JEM-2800F), atomic force microscopy (AFM, Bruker Dimension ICON), aberration-corrected high-angle annular dark field scanning TEM (AC HAADF-STEM, Themis Z, FEI) equipped with energy-dispersive X-ray spectroscopy (EDS) mapping at an accelerating voltage of 200 kV, and X-ray diffraction (XRD, Rigaku XtalAB PRO MM007 DW). N$_2$ adsorption/desorption isotherms were obtained by using Micromeritics ASAP 2460 Surface Area and Porosity Analyzer. The surface chemical composition and elementary chemical states were studied by X-ray photoelectron spectroscopy (XPS, Thermo Scientific ESCALAB 250Xi). The element content was determined by inductively coupled plasma optical emission spectroscopy (ICP-OES, Agilent 725ES & Agilent 5110). The degree of graphitization of electrocatalysts was studied by Raman spectroscopy (Horiba Scientific LabRAM HR Evolution). X-ray absorption spectra (XAS) including X-ray absorption near-edge structure (XANES) and extended X-ray absorption fine structure (EXAFS) at Ni K-edge were collected at the Beamline of TLS07A1 in National Synchrotron Radiation Research Center (NSRRC), Hsinchu.

2.3. Electrochemical measurements

All electrochemical tests were performed in CO$_2$-saturated 0.5 M KHCO$_3$ electrolyte at ambient temperature and pressure with a customized gastight H-type glass cell (Gaoss Union) separated by Nafion 117 membrane and a CHI760E potentiostat. In a typical 3-electrode test, a platinum foil (1 × 1 cm^2) and an Ag/AgCl electrode were used as the counter and reference electrode, respectively. A commercial glassy carbon (GC) electrode (5 mm in diameter, 0.196 cm^2) was used as the working electrode. To prepare the catalyst ink, 5 mg of catalyst and 50 μl

of 5 wt% Nafion solution, 500 μl of distilled water and 450 μl of ethanol were mixed and sonicated for 30 min. Then 4 μl of the catalyst ink was applied onto the glassy carbon electrode and allowed to dry in air, giving a catalyst loading of 0.1 mg cm^{-2}. A certain amount of KHCO$_3$ (99.95%, Sigma-Aldrich) was dissolved in distilled water to prepare the 0.5 M electrolyte. A CO$_2$-saturated electrolyte (pH=7.2) was prepared by purging CO$_2$ (99.99%, Air Liquide) into 0.5 M KHCO$_3$ aqueous solution for 30 min before tests, and a flow of CO$_2$ was stabilized at 10 sccm during the electrochemical measurements. Cyclic voltammetry (CV) was performed at a scan rate of 50 mV s^{-1}, and linear sweep voltammetry (LSV) was recorded at a scan rate of 5 mV s^{-1}. The electrolytes were constantly stirred at 900 rpm during LSV tests. All potentials in this work were normalized to RHE according to the Nernst equation ($E_{RHE} = E_{Ag/AgCl} + 0.198 + 0.059 \times pH$).

The TOF (h^{-1}) of product CO was evaluated as follows:

$$TOF\ (h^{-1}) = CO_{molecule/h}/Ni_{atom} = I \times t \times FE_{CO} \times M_{Ni}/(2 \times m_{catalyst} \times w_{Ni} \times F)$$

where $CO_{molecule/h}$ is the number of CO molecules produced in 1 h; Ni_{atom} is the number of nickel sites on the catalyst; I is the current density at a given potential; t is the reaction time; FE_{CO} is the faradaic efficiency of CO; M_{Ni} is the molecular weight of nickel; $m_{catalyst}$ is the catalyst weight; w_{Ni} is the mass fraction of nickel on the catalyst; and F is the faradaic constant (96,485 C/mol).

CO$_2$ reduction was conducted in a flow cell with the catalyst coated on a gas diffusion electrode (GDE). The CO$_2$ gas flow rate was set to 20 sccm, and 1 M KHCO$_3$ solution was used as both the catholyte and the anolyte. Anion exchange membranes were used to separate the cathode and anode chambers. Ni foam was used as the anode (counter electrode). The cathode potentials were measured against Ag/AgCl reference electrode.

2.4. Analyses for CO$_2$RR products

The CO$_2$RR products were analyzed in the above-mentioned system, but the working electrode was replaced. To prepare the working electrode, the catalyst ink was dripped onto a carbon fiber paper (1 cm^2) with a mass loading of 0.2 mg cm^{-2}. The gaseous products were quantified by a gas chromatograph (GC, SCION-456GC) equipped with thermal conductivity detector (TCD) for H$_2$ detection and flame ionization detector (FID) for CO and CH$_4$. Ultra-pure helium (He, 99.9999%) was used as the carrier gas. The flow rate of CO$_2$ was stabilized at 10 sccm at the inlet of the electrochemical cell with a standard series mass flow controller (Alicat Scientific mc-100 sccm) during CO$_2$RR experiments. Quantification of gas products was calculated with external gas standard. Liquid products were detected by high performance liquid chromatography (HPLC, Agilent 1260 Infinity II).
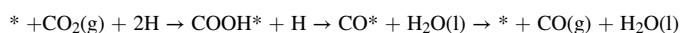
The faradaic efficiency of gaseous products was calculated as the following equation: $FE_{product} = \frac{Q_{product}}{Q_{total}}$, the faradaic efficiency of CO can be calculated as follows: $FE_{CO} = \frac{2F \times n_{CO}}{I \times t}$, the number 2 means that two electrons are needed to produce one CO molecule, F is the Faraday constant (96,485 C/mol), n_{CO} is the total amount of CO produced which was measured by gas chromatography, I is the reduction current at a specific applied potential, and t is the time for the constant reduction current.

2.5. Computational details

The spin-polarized energy calculations were performed by using density functional theory methods implemented in the Vienna Ab initio Simulation Package (VASP) [14]. The GGA-PBE exchange-correlation functional was utilized to optimize all the structures and the dispersion correction (D3-Grimme) was employed to better describe the weak interactions [15,16]. We set a cutoff energy of 450 eV for plane-wave basis set, and used the energy and force convergence of 10^{-4} eV and 0.05 eV/Å for geometric optimization. The Brillouin zones were

sampled with $3 \times 3 \times 1$ and $2 \times 2 \times 1$ for $3 \times 5 \times 1$ and $4 \times 7 \times 1$ supercells, respectively. The vacuum space larger than 15 Å was set along the z-axis.

The formation energy of Ni/Ni_{10} doped defect-Ni-N$_3$ was calculated by $E_f = E_{total} - E_{base} - E_{Ni/Ni10}$, where E_{total} and E_{base} denote the energies of Ni/Ni_{10} doped and undoped system, and $E_{Ni/Ni10}$ represents the energy of single Ni atom or Ni_{10} cluster in vacuum. For the involved reactions in this work, we considered both the reaction mechanisms of CO_2RR and HER. The involved reactions are as follows:

$$* + CO_2(g) + 2H \rightarrow COOH^* + H \rightarrow CO^* + H_2O(l) \rightarrow * + CO(g) + H_2O(l)$$

$$* + 2H \rightarrow 2H^* \rightarrow * + H_2(g)$$

The free energy changes of intermediates mentioned above were derived from $G = E + Ezpe + EH – TS$, and the free energy correction of adsorbed intermediates was calculated based on the VASPKIT tool at 298.15 K [17]. For gas (CO_2 and CO) molecules, we made corresponding correction according to the experiment due to the inaccuracy of PBE [18–20]. The free energies of species (H_2O, CO, and CO_2) are listed in Table S1. The dielectric constant was set as 78.54 to simulate the H_2O environment [21]. For some typical structures, such as NiN_3Vac and NiN_4, we also considered and compared the effects of explicit solvents. We added 36 H_2O molecules with the density of 1 g/cm^{-3} in the supercell (vacuum layer > 10 Å).

3. Results and discussion

3.1. Materials preparation and characterization

In a typical synthesis (Scheme 1), glucose, L-alanine and nickel(II) acetate tetrahydrate were uniformly mixed with sodium carbonate and placed in a corundum boat. Then the corundum boat was put into a special mechanical reciprocating device which can shift from the cooling to the heating zone rapidly. Typically, the reactants were fast pyrolyzed at a high temperature of 1000 °C in an Ar atmosphere for 90 s. After fast pyrolysis, the products were washed thoroughly to remove sodium carbonate. Besides, subsequent thermal annealing was used to increase the conductivity of the final product Ni-SAC@NC. To make comparison, the Ni single-atom catalyst supported on carbon (Ni-SAC@C), the pure carbon sample (C) and nitrogen doped carbon sample (N-C) were also synthesized by adjusting the composition of the precursors.

Through SEM images, the samples all exhibit similar porous three-dimensional network structure (Figs. 1a, and S3), indicating the universality of our method. AFM and TEM images prove that Ni-SAC@NC has a few-layer graphene structure, and the curved lattice fringes in the high-solution TEM (HRTEM) images prove the high crystallization of the sample (Figs. 1b, c and S4a). The STEM images and corresponding elemental mapping demonstrate the uniform distribution of C, N and Ni elements (Fig. 1d). As shown in Figs. 1e and S5a, the HAADF-STEM images prove the uniform distribution of Ni atoms in Ni-SAC@NC and Ni-SAC@C, as well as abundant pores (dark black area) marked by red circles. Each bright spot corresponds to an isolated Ni atom with a diameter of about 0.2 nm in the substrate. Ni-SAC@NC has more bright

spots than Ni-SAC@C, which indicates that the former has a higher Ni content (Fig. S6). The addition of N element improves the ability of the substrate to anchor Ni atoms. The uniform dispersion of different elements in the carbon frame was also confirmed by mapping Figs. S4b and S5b. EDS (Figs. S4c and S5c) also proves the existence of Ni element. The above studies have proved the successful preparation of Ni SACs.

During the preparation, fast pyrolysis is key to form atomically dispersed Ni. The sudden high temperature will cause a large amount of gases from the decomposition of carbon-containing precursors to generate high internal pressure. The instantaneous high internal pressure can inhibit the agglomeration of Ni atoms from the decomposition of nickel(II) acetate tetrahydrate to achieve high dispersion of Ni atoms. The produced N atoms from L-alanine can further fix Ni atoms via Ni-N coordination. All intrinsically promote the formation of Ni SACs [22]. All experimental conditions are optimal (Figs. S7–S11). DFT computations also demonstrate that the synthetic environment with high pressure and temperature can facilitate the formation of single atoms. In this work, we first discussed the effects of stress on the formation energy of single atoms. As shown in Fig. S12, we show the formation energies of Ni single-atom anchored in defective NC under pressure of −4% to 4%. The formation energies of single atoms become more negative when the compressive pressure is applied, which proves that the pressure can promote the synthesis of materials. In addition, by using ab initio molecular dynamics simulations, we explored the effect of temperature by simulating the synthetic route, which is illustrated in Fig. S12c. Nickel atoms would be anchored at the vacancies at the temperature of 1000 K, whereas nickel(II) acetate could not break completely under 300 K, suggesting that high temperature is conducive to the formation of single atom. With the high surface energy of the isolated single metal atoms on the support, the metal atoms tend to agglomerate during the preparation [23], and a suitable preparation method is essential. Compared with the traditional and widely used pyrolysis method, the fast pyrolysis method can intrinsically inhibit the agglomeration of metals and promote the high dispersion of metal atoms. We also used non-fast pyrolysis method to prepare Ni-N-C material, and performed XRD and SEM. Ni metal peaks can be observed in the XRD patterns, and obvious metal particles can also be observed in the SEM image (Fig. S13). This further demonstrates the importance of fast pyrolysis method for the formation of single-atom catalysts. Compared with some bottom-up synthesis techniques such as coprecipitation, atomic layer deposition and photochemical reduction [24], the fast pyrolysis method is easy to operate and does not require expensive raw materials including metal-organic frameworks (MOFs) and precursors [25].

XRD was used to identify the components of the as-prepared samples, only carbon (002) and (004) diffraction peaks are observed at 14.2° and 44.0°, respectively (Fig. 2a) [26]. The Ni-containing samples have stronger and sharper diffraction peaks, indicating that the addition of Ni enhances the crystallization [22]. This is further proved by Raman spectra; Ni-SAC@NC and Ni-SAC@C have lower I_D/I_G values than N-C (Fig. S14a).

BET surface area, pore volume and average pore size of Ni-SAC@NC are 569.31 m^2 g^{-1}, 2.24 cm^3 g^{-1} and 15.71 nm, respectively. As shown in Fig. 2b, the isotherm is classified as type-IV, with a hysteresis loop of type-H4, indicating the presence of numerous mesopores in Ni-SAC@NC. As shown in the inset of Fig. 2b, the mesopores exhibit obvious peaks at 2.5 nm, 3.8 nm and 36.6 nm. The isothermal adsorption-desorption curve of the sample containing micropores will have a relatively high adsorption capacity in the low-pressure range, as shown in Fig. 2b, so we also used the Horvath-Kawazoe method to get the pore size distribution of micropores. The pore diameter corresponding to the highest point of the ordinate is the most concentrated pore in the micropore range. As shown in Fig. S14b, the median pore width of micropores is 1.10 nm. The micropores and mesopores are most probably caused by the release of small gas molecules or the activation of sodium carbonate. Together with macropores caused by the removal of sodium carbonate templates, Ni-SAC@NC shows a hierarchical pore
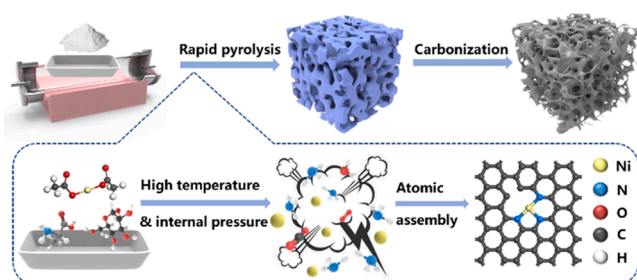
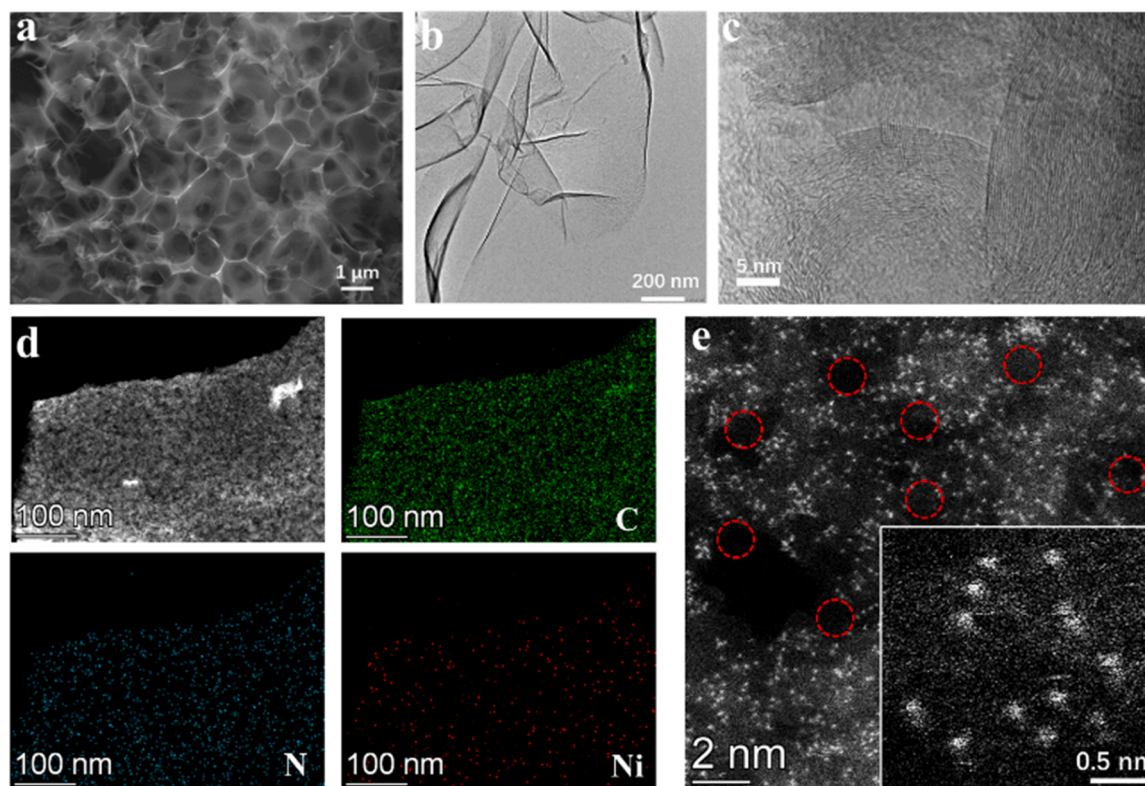**Scheme 1.** Schematic illustration of the preparation of Ni-SAC@NC.

Fig. 1. a) SEM, b) TEM and c) HRTEM images of Ni-SAC@NC. d) STEM images and corresponding elemental mapping images of C, N, and Ni of Ni-SAC@NC. e) HAADF-STEM image of Ni-SAC@NC.

structure. The large specific surface area can expose more accessible active sites while the hierarchical pore distribution can reduce the mass transport distance and promote mass transport. The defects generated by the abundant pore structure will further affect the coordination environment of Ni single atoms and thus affect the catalytic performance, which will be discussed later. The elemental composition of the sample is further indicated by the full spectrum of XPS (Fig. S14c). Small Ni peaks can be observed in the full spectrum of Ni-SAC@NC. The nitrogen content is 3.28 and 6.52 wt% in N-C and Ni-SAC@NC, respectively. The content of Ni determined by XPS is 1.28 and 2.34 wt% in Ni-SAC@C and Ni-SAC@NC, respectively, which are close to those obtained by ICP-OES (1.49 and 2.54 wt%, respectively). More Ni atoms as the center fixed by N in the graphene substrate further catalyze the growth of graphene (Ni-containing samples have higher crystallization than non-Ni samples, which explains the previous results of XRD and Raman). Due to the lack of nitrogen, C and O elements have less fixation effect on Ni atoms, and the isolated Ni content of Ni-SAC@C is smaller, which is consistent with the results by HAADF-STEM and ICP-OES. The detailed N1s spectrum of Ni-SAC@NC can be deconvoluted into five representative atomic bonded peaks at 398.2 eV, 399.5 eV, 400.5 eV, 401.3 eV and 403.5 eV, corresponding to pyridinic-N, Ni-N, pyrrolic-N, graphitic-N and oxidized-N, respectively (Fig. 2c). By analyzing the Ni2p curve of Ni-SAC@NC (Fig. 2d), two peaks at 855.0 eV and 872.5 eV correspond to $Ni2p_{3/2}$ and $Ni2p_{1/2}$, respectively. The binding energies of Ni $2p_{3/2}$ is lower than that of Ni^{2+} (856.0 eV) and higher than that of Ni^{0} (853.5 eV), which suggests that the Ni atom in Ni-SAC@NC is in a low-valence state between 0 and +2 [27].

Synchrotron X-ray absorption spectroscopy was used to explore the coordination environment of Ni atoms. Fig. 2e shows the typical XANES of the Ni K-edge of different samples. The energies of pre-edge of Ni-SAC@NC and Ni-SAC@C are located between Ni foil and NiO, which means that the oxidation states of Ni single atoms are between Ni(0) and Ni(II), in accordance with the XPS results. The k^2-weighted Fourier

transforms of the EXAFS at the Ni K-edge were further used to explore the possible coordination environment around Ni single atoms. As shown in Fig. 2f, Ni-O and Ni-O-Ni interaction of NiO locate at 1.58 Å and 2.53 Å, respectively. Ni-Ni interaction of Ni foil locates at 2.13 Å. Nickel phthalocyanine (NiPc) displays the main peaks around 1.46 Å, which can be assigned to the scattering interaction between the Ni atoms and the first shell (Ni-N). Notably, the main peak of Ni-SAC@NC is 1.41 Å, which is shorter than that of NiPc, indicating that the coordination environment of Ni in Ni-SAC@NC is different from the $Ni-N_4$ coordination of NiPc. Moreover, the intensity of the peak at 1.41 Å in Ni-SAC@NC is lower than that of NiPc, probably due to the formation of unsaturated $Ni-N_2$ and $Ni-N_3$ species [28]. The peak related to Ni-Ni bonds in Ni foil is not observed in the profile of Ni-SAC@NC, suggesting the formation of uniformly dispersed Ni atoms, in accordance with the XRD results and HAADF-STEM image. Ni-SAC@C shows the main peaks around 1.60 Å, which can be assigned to the Ni-—O bonds. Considering that the high-energy Ni-O coordination may lead to the destruction of the structure, we speculate that Ni atoms in Ni-SAC@C are fixed in the carbon substrate by the coordination of C and O together [29,30]. The wavelet transform (WT) at the Ni K-edge was also adopted to explore the atomic configuration in Ni-SAC@NC (Fig. 2g–i) because of the high resolution in both k and R spaces. After complex wavelet development, a signal composed of slowly varying amplitude term and a fast oscillating phaseterm can be obtained [31]. Compared with the WT plots of Ni foil, the plots of Ni-SAC@NC display the intensity maximum at 4.2 Å^{-1}, which can be attributed to the Ni-N pair, and the signal of Ni-Ni pair (8.0 Å^{-1}) was not detected. This indicates the monodispersion of Ni atoms in Ni-SAC@NC. Moreover, the intensity maximum of Ni-SAC@NC shows a lower k value than that of Ni-O-Ni in NiO, further indicating the possibility of the existence of Ni-—N bonds in the sample [32]. First shell fitting for Ni-SAC@NC shows Ni coordination numbers of 3.1 and Ni-—N bond length of 1.89 Å (Table S2). The number of the nearest N atoms coordinated to Ni was found to be three and a large
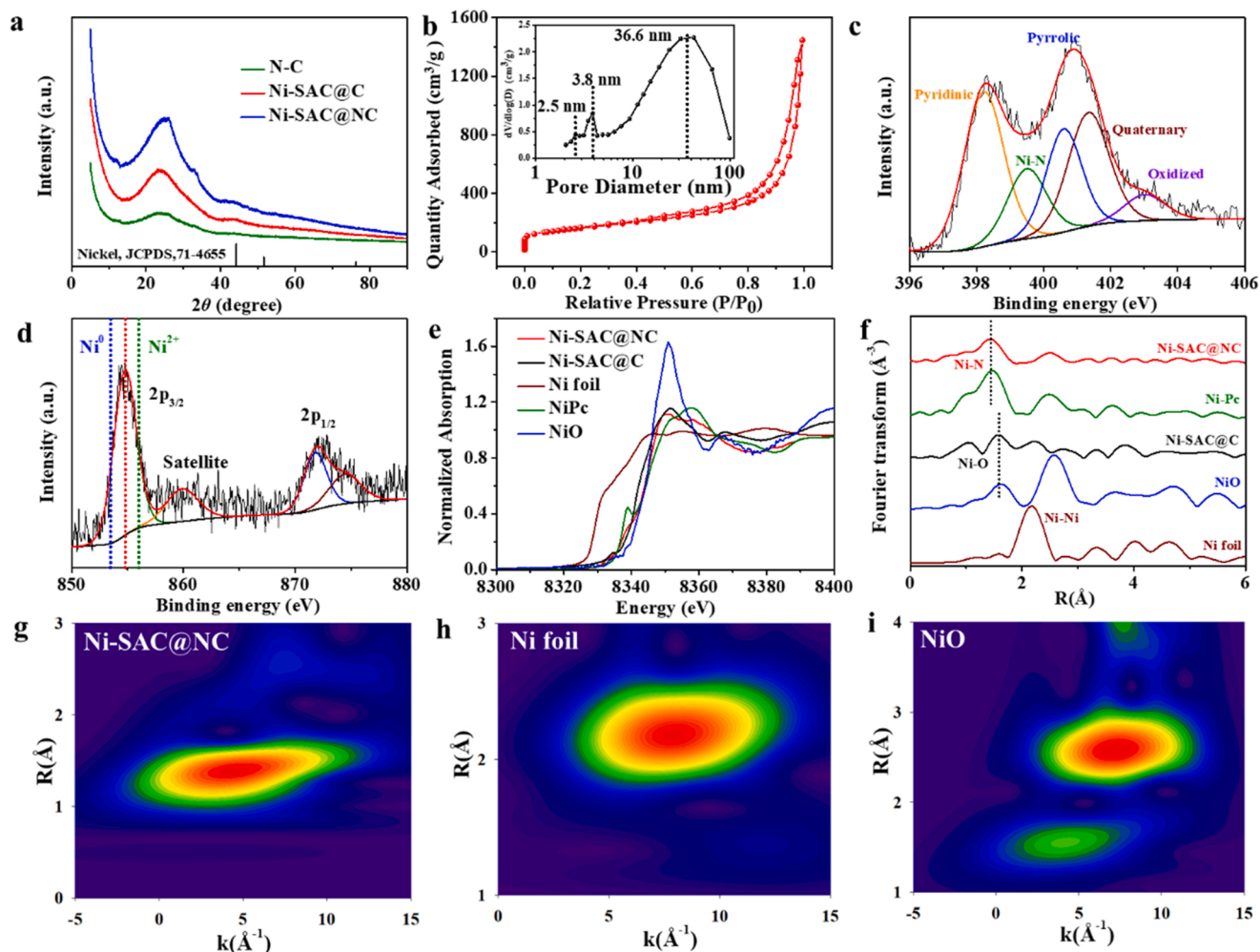
Fig. 2. a) XRD patterns of the samples. b) N_2 adsorption-desorption isotherm curves of Ni-SAC@NC. Inset is the pore distribution curve. c), d) High-resolution XPS N1s and Ni2p spectra of Ni-SAC@NC. e) Ni K-edge XANES spectra of the samples. f) Fourier transformation of EXAFS spectra of the samples. g)-i) WT-EXAFS plots of Ni-SAC@NC, Ni foil and NiO, respectively.

number of defect structures proved by HRTEM images, BET tests and pore structure analysis inevitably affect the coordination environment of Ni atoms; thus we speculate that Ni-SAC@NC may be a defect-Ni-N_3 structure. This structure can well be matched with the previous XANES and Fourier transforms of EXAFS results and will be further verified by DFT computations in the following section.

3.2. Electrochemical performance

The electrochemical activity of CO_2RR was tested for the obtained samples by CV and LSV under three-electrode systems. As shown in the CV curves (Fig. 3a), the current density of Ni-SAC@NC under CO_2 atmosphere is much higher than that under Ar atmosphere, which shows the effective CO_2 electrochemical reduction activity of the sample. In the LSV tests of the four samples (Fig. 3b), N-C and Ni-SAC@C exhibit higher current density than C, which means that the addition of N atoms and Ni atoms improves the CO_2 electrochemical reduction activity of pure C materials. However, the current densities of N-C and Ni-SAC@C are significantly lower than that of Ni-SAC@NC, suggesting the great importance of the joint participation of Ni, N and C to the promotion of CO_2 electrochemical reduction activity. Ni-SAC@NC also shows the lowest onset potential among the four samples. The calculated TOF of Ni-SAC@NC reaches 2400 h^{-1} at an overpotential of 0.5 V and 5200 h^{-1} at an overpotential of 0.6 V, which are comparable to some advanced electrocatalysts for electrochemical reduction of CO_2 to CO (Table S3).

As shown in Fig. 3c, the Tafel slope of Ni-SAC@NC is 138 mV decade^{-1} and much lower than that of Ni-SAC@C, suggesting the favorable kinetics of Ni-SAC@NC for the reduction of CO_2 [33]. Online GC and offline HPLC were used to detect the gaseous and liquid products of CO_2RR, respectively. Only the presence of CO and H_2 was detected, and no liquid product was detected (Fig. S15). As shown in Figs. 3e and S16, the CO_2-to-CO faradaic efficiency of Ni-SAC@NC keeps well above 80% in the applied potential window of −0.6 to −0.9 V (vs. RHE), with a highest FE_{CO} of 95% at 0.6 V (vs. RHE). This almost completely surpasses the representative precious metal Au catalyst which can reduce CO_2 to CO effectively. N-C exhibits a poor activity for CO_2 reduction, suggesting the important role of Ni atoms in catalyzing the conversion of CO_2 into CO. Moreover, the maximum FE_{CO} of Ni-C is only 39%, which may be due to the lack of nitrogen atoms leading to a lower content of highly dispersed Ni atoms on the graphene substrate and unsuitable electron transfer [30]. The C sample shows poor performance in CO_2RR, and a small amount of CO was detected in the full voltage range. As shown in Fig. 3e, the FE of hydrogen produced by Ni-SAC@NC is much lower than those of C, N-C and Ni-SAC@C samples, indicating that the competitive hydrogen evolution reaction is greatly inhibited over the single Ni-N sites. Compared with the reported advanced Ni SACs (Table S3), Ni-SAC@NC can even achieve the best CO selectivity under a smaller overpotential, which also surpasses most other non-single-atom catalysts (Fig. 3f). The stability test was also performed. The Ni-SAC@NC sample can work for 10 h at a potential of 0.6 V (vs. RHE)
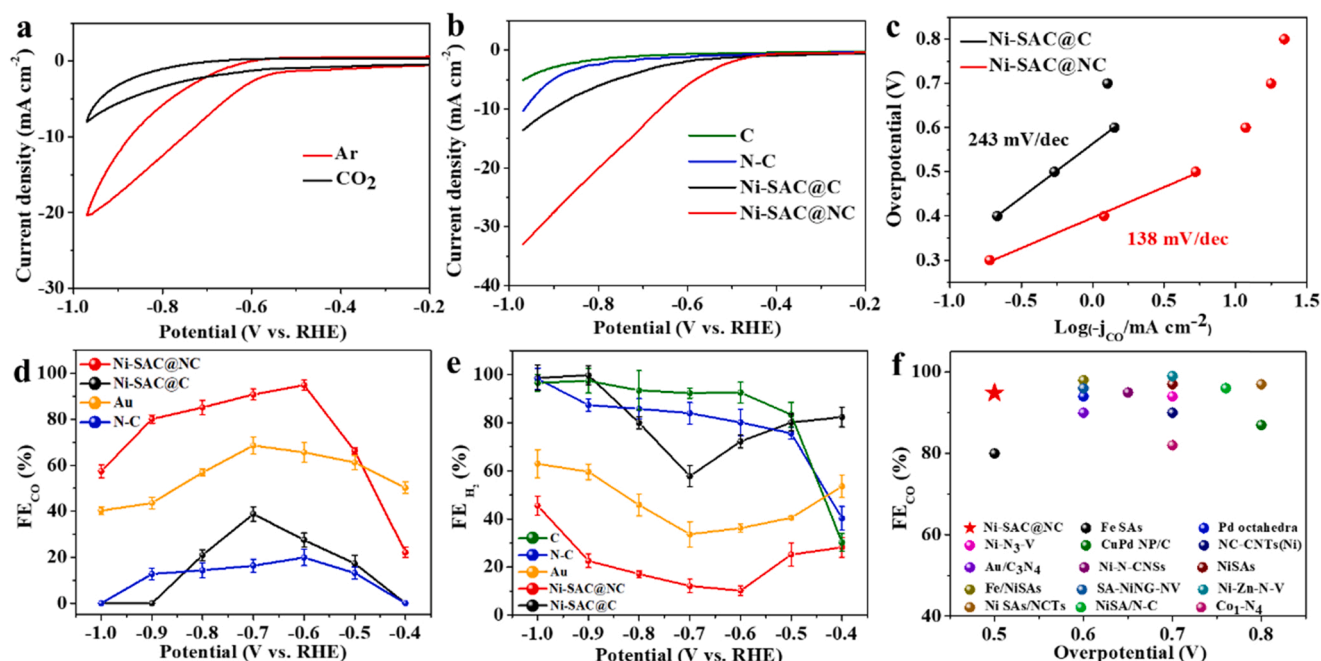
Fig. 3. a) CV curves of Ni-SAC@NC on glassy carbon electrodes in Ar and CO_2 saturated 0.5 M $KHCO_3$ at a scan rate of 50 mV s^{-1}. b) LSV curves measured in the CO_2 saturated 0.5 M $KHCO_3$ electrolyte. c) Tafel plots for producing CO. d) FE curves for CO. e) FE curves for H_2. f) FE_{CO} of Ni-SAC@NC (marked as a red star) compared with those of other advanced CO_2 to CO reduction catalysts (Table S3). (For interpretation of the references to color in this figure legend, the reader is referred to the web version of this article.)

and the FE_{CO} remained stable. We compared the SEM image and XRD patterns of the catalyst coated on carbon paper before and after the stability test, which did not show the obvious evidence of the changes of Ni sites, showing the superior stability of the catalyst (Fig. S14d–f). The CO_2 electroreduction activity of Ni-SAC@NC was also evaluated onto a gas diffusion electrode (GDE) in a flow cell with 1.0 M $KHCO_3$ as the electrolyte, where a CO partial current of 187.7 mA cm^{-2} was obtained at 2.7 V cell voltage. FE_{CO} reached the maximum value 96.6% at 1.7 V (Fig. S17). The above results indicate that Ni-SAC@NC has excellent performance and stability during CO_2RR. The use of SACs for electrocatalytic reactions and advanced characterization methods have important research significance [34–39]. Our work would provide a guideline for the design and characterization of SACs.

3.3. Computational insights

DFT computations were also performed to further understand the CO_2RR activities of Ni-SAC@NC and Ni-SAC@C. According to the EXAFS fitting results that Ni-SAC@NC may be a defect-Ni-N$_3$ structure in experiments, we first considered the NiN$_3$Vac structure with a Ni metal atom coordinated by three nitrogen atoms and one vacancy. The Ni-—N bond length of this structure is 1.87 Å, which is in good agreement with the experimental value (1.89 Å). As for Ni-SAC@C, we added an O atom because of the existence of Ni-—O bonding in experiments. The specific structures of NiN$_3$Vac and Ni-SAC@C without N doping, namely NiC$_2$OVac, are shown in Fig. 4a and b. In addition, it has been proved that NiN$_4$ (Fig. 4c) shows good activity and selectivity in CO_2RR [27,40]; therefore, we compared the free energy diagrams of the NiC$_2$OV, NiN$_3$Vac and NiN$_4$ by adding three explicit water layers to simulate the water-solid interface. As shown in Fig. 4d, NiN$_3$Vac is conducive to the generation of COOH* and its free energy barrier of the potential-determining step (COOH* → CO*) is 0.62 eV. For the structure of NiC$_2$OVac, although the free energy barrier is only 0.44 eV (* + CO_2 → COOH*), the CO* is difficult to desorb and the surface of catalysts is easy to be poisoned. As for NiN$_4$, the formation of COOH* faces a higher free energy barrier (1.19 eV). The computations imply that NiN$_3$Vac

shows the best catalytic activity to produce CO.

To better understand the selectivity of CO_2RR, the competitive HER of NiN$_3$Vac and NiC$_2$OVac were also calculated. As shown in Fig. S18, the ΔG of NiN$_3$Vac and NiC$_2$OVac are 0.42 eV and 0.79 eV, respectively. Large values of ΔG (much greater than 0 eV) exhibit poor HER activity, indicative of increased selectivity of CO [41–43]. In general, DFT computations are consistent with the experiments, and provide important and supporting insights to explain why NiN$_3$Vac has excellent CO_2RR activity and selectivity.

4. Conclusion

We successfully prepared Ni SACs via an effective strategy of fast pyrolysis, which can intrinsically inhibit the agglomeration of metal atoms to achieve high dispersion of Ni atoms. Compared with the control samples, Ni-SAC@NC shows the best performance for CO_2RR. The FE_{CO} keeps well above 80% in the applied potential window of −0.6 to −0.9 V (vs. RHE), with a highest FE_{CO} of 95% at −0.6 V (vs. RHE). The CO partial current of 187.7 mA cm^{-2} was obtained at 2.7 V cell voltage and FE_{CO} reached 93.8% under flow cell tests. The performance surpasses most advanced CO_2RR catalysts and provides a solution for carbon neutralization. DFT computations indicate that the defect-Ni-N$_3$ structure is the highly active site in Ni-SAC@NC for CO_2RR. This work develops a new route to prepare single-atom catalysts and proves the important roles of metal centers and coordination environment in electrocatalytic processes.

CRediT authorship contribution statement

The manuscript was written through contributions of all authors. All authors have given approval to the final version of the manuscript. **Y.B. Guo, H.J. Cui, Z. Zhou:** Conceptualization. **Y.B. Guo, S. Yao, H.J. Cui, Z. Zhou:** Methodology. **Y.B. Guo, S. Yao, Y.Y. Xue, X. Hu:** Investigation. **Y.B. Guo, S. Yao, Y.Y. Xue, X. Hu:** Data curation. **Y.B. Guo:** Writing – original draft. **Y.B. Guo, S. Yao, Y.Y. Xue, X. Hu, H.J. Cui, Z. Zhou:** Writing – review & editing. **H.J. Cui, Z. Zhou:** Supervision. **Z.**
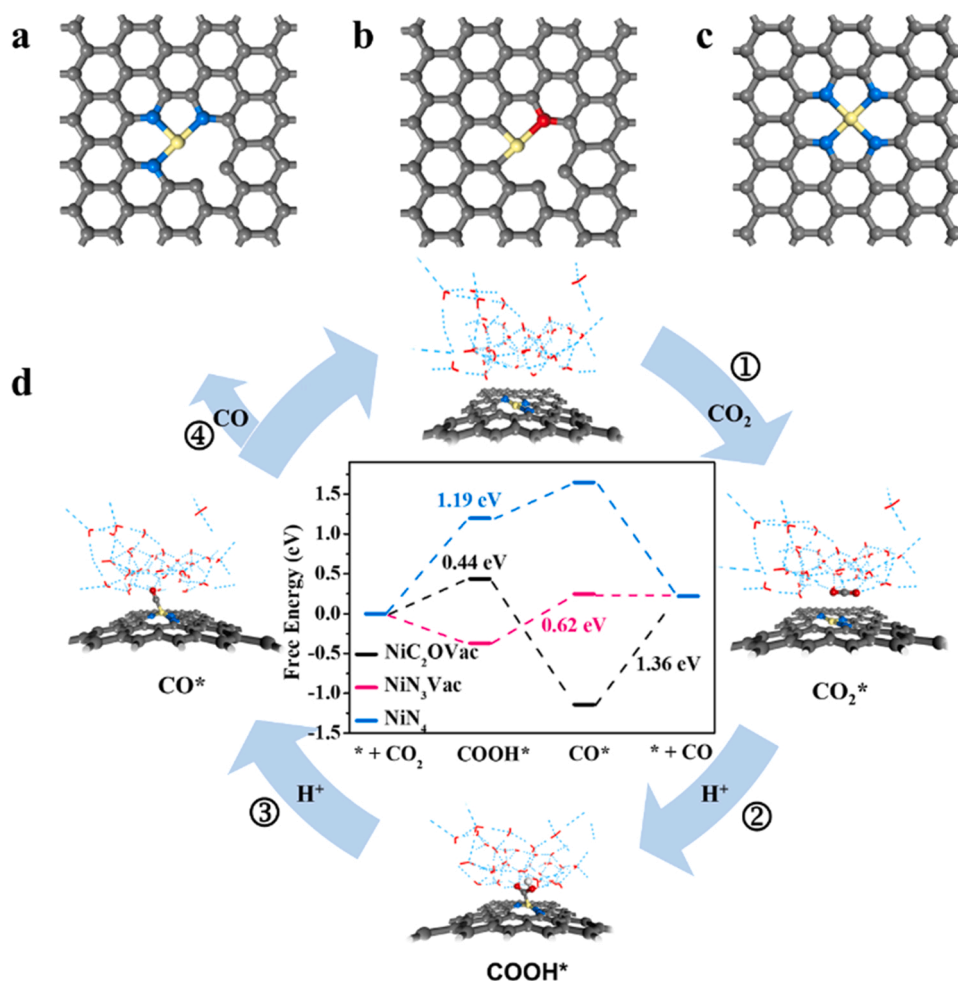
Fig. 4. The structures of a) NiN_3Vac, b) NiC_2OVac and c) NiN_4. The gray, blue, yellow and red atoms represent carbon, nitrogen, nickel and oxygen, respectively. d) The proposed reaction pathways and free energy diagrams for electrochemical reduction of CO_2 to CO. (For interpretation of the references to color in this figure legend, the reader is referred to the web version of this article.)

Zhou: Funding acquisition.

Declaration of Competing Interest

The authors declare that they have no known competing financial interests or personal relationships that could have appeared to influence the work reported in this paper.

Acknowledgements

Appendix A. Supporting information

Supplementary data associated with this article can be found in the online version at doi:10.1016/j.apcatb.2021.120997.

References

[1] Y.Y. Birdja, E. Pérez-Gallent, M.C. Figueiredo, A.J. Göttle, F. Calle-Vallejo, M.T. M. Koper, Advances and challenges in understanding the electrocatalytic conversion of carbon dioxide to fuels, Nat. Energy 4 (2019) 732–745.

[2] H. Cui, Y. Guo, L. Guo, L. Wang, Z. Zhou, Z. Peng, Heteroatom-doped carbon materials and their composites as electrocatalysts for CO2 reduction, J. Mater. Chem. A 6 (2018) 18782–18793.

[3] X.-L. Lu, X. Rong, C. Zhang, T.-B. Lu, Carbon-based single-atom catalysts for CO2electroreduction: progress and optimization strategies, J. Mater. Chem. A 8 (2020) 10695–10708.

[4] Q. Fan, P. Hou, C. Choi, T.S. Wu, S. Hong, F. Li, Y.L. Soo, P. Kang, Y. Jung, Z. Sun, Activation of Ni particles into single Ni–N atoms for efficient electrochemical reduction of CO2, Adv. Energy Mater. 10 (2019), 1903068.

[5] D.M. Koshy, A.T. Landers, D.A. Cullen, A.V. Ievlev, H.M. Meyer, C. Hahn, Z. Bao, T. F. Jaramillo, Direct characterization of atomically dispersed catalysts: nitrogen-coordinated Ni sites in carbon-based materials for CO2 electroreduction, Adv. Energy Mater. 10 (2020), 2001836.

[6] Z. Li, D. He, X. Yan, S. Dai, S. Younan, Z. Ke, X. Pan, X. Xiao, H. Wu, J. Gu, Size-dependent nickel-based electrocatalysts for selective CO_2 reduction, Angew. Chem. Int. Ed. 59 (2020) 18572–18577.

[7] W. Ju, A. Bagger, G.P. Hao, A.S. Varela, I. Sinev, V. Bon, B. Roldan Cuenya, S. Kaskel, J. Rossmeisl, P. Strasser, Understanding activity and selectivity of metal-nitrogen-doped carbon catalysts for electrochemical reduction of CO_2, Nat. Commun. 8 (2017) 944.

[8] Y. Pan, R. Lin, Y. Chen, S. Liu, W. Zhu, X. Cao, W. Chen, K. Wu, W.C. Cheong, Y. Wang, L. Zheng, J. Luo, Y. Lin, Y. Liu, C. Liu, J. Li, Q. Lu, X. Chen, D. Wang, Q. Peng, C. Chen, Y. Li, Design of single-atom Co-N5 catalytic site: a robust electrocatalyst for CO_2 reduction with nearly 100% CO selectivity and remarkable stability, J. Am. Chem. Soc. 140 (2018) 4218–4221.

[9] X. Rong, H.J. Wang, X.L. Lu, R. Si, T.B. Lu, Controlled synthesis of a vacancy-defect single-atom catalyst for boosting CO_2 electroreduction, Angew. Chem. Int. Ed. 59 (2020) 1961–1965.

[10] H. Xu, D. Rebollar, H. He, L. Chong, Y. Liu, C. Liu, C.-J. Sun, T. Li, J.V. Muntean, R. E. Winans, D.-J. Liu, T. Xu, Highly selective electrocatalytic CO_2 reduction to ethanol by metallic clusters dynamically formed from atomically dispersed copper, Nat. Energy 5 (2020) 623–632.

[11] Y. Guo, Y.-N. Chen, H. Cui, Z. Zhou, Chin. J. Catal. 40 (2019) 1298–1310.

[12] H. Cui, Y. Guo, W. Ma, Z. Zhou, 2 D materials for electrochemical energy storage: design, preparation, and application, ChemSusChem 13 (2020) 1155–1171.

[13] S. Liu, H.B. Yang, S.F. Hung, J. Ding, W. Cai, L. Liu, J. Gao, X. Li, X. Ren, Z. Kuang, Y. Huang, T. Zhang, B. Liu, Elucidating the electrocatalytic CO2 reduction reaction over a model single-atom nickel catalyst, Angew. Chem. Int. Ed. 132 (2019) 808–813.

[14] G. Kresse, J. Hafner, Ab initio molecular dynamics for liquid metals, Phys. Rev. B Condens. Matter 47 (1993) 558–561.

[15] L.F. Lai, J.R. Potts, D. Zhan, L. Wang, C.K. Poh, C.H. Tang, H. Gong, Z.X. Shen, L. Y. Jianyi, R.S. Ruoff, Exploration of the active center structure of nitrogen-doped graphene-based catalysts for oxygen reduction reaction, Energy Environ. Sci. 5 (2012) 7936–7942.

[16] S. Grimme, J. Antony, S. Ehrlich, H. Krieg, A consistent and accurate ab initio parametrization of density functional dispersion correction (DFT-D) for the 94 elements H-Pu, J. Chem. Phys. 132 (2010), 154104.

[17] V. Wang, N. Xu, J.C. Liu, G. Tang, W.T. Geng, VASPKIT: a user-friendly interface facilitating high-throughput computing and analysis using VASP code, Comput. Phys. Commun. 267 (2021), 108033.

[18] F. Calle-Vallejo, M.T.M. Koper, Theoretical considerations on the electroreduction of CO to C2 species on Cu(100) electrodes, Angew. Chem. Int. Ed. 125 (2013) 7423–7426.

[19] M. Fishman, H.L.L. Zhuang, K. Mathew, W. Dirschka, R.G. Hennig, Accuracy of exchange-correlation functionals and effect of solvation on the surface energy of copper, Phys. Rev. B 87 (2013), 245402.

[20] A.A. Peterson, F. Abild-Pedersen, F. Studt, J. Rossmeisl, J.K. Norskov, How copper catalyzes the electroreduction of carbon dioxide into hydrocarbon fuels, Energy Environ. Sci. 3 (2010) 1311–1315.

[21] K. Mathew, R. Sundararaman, K. Letchworth-Weaver, T.A. Arias, R.G. Hennig, Implicit solvation model for density-functional study of nanocrystal surfaces and reaction pathways, J. Chem. Phys. 140 (2014), 084106.

[22] D.M. Koshy, S. Chen, D.U. Lee, M.B. Stevens, A.M. Abdellah, S.M. Dull, G. Chen, D. Nordlund, A. Gallo, C. Hahn, D.C. Higgins, Z. Bao, T.F. Jaramillo, Understanding the origin of highly selective CO2 electroreduction to CO on Ni,N-doped carbon catalysts, Angew. Chem. Int. Ed. 59 (2020) 4043–4050.

[23] C. Zhu, S. Fu, Q. Shi, D. Du, Y. Lin, Single-atom electrocatalysts, Angew. Chem. Int. Ed. 56 (2017) 13944–13960.

[24] Q. Zhang, J. Guan, Single-atom catalysts for electrocatalytic applications, Adv. Funct. Mater. 30 (2020), 2000768.

[25] Y. Zhang, L. Guo, L. Tao, Y. Lu, S. Wang, Defect-based single-atom electrocatalysts, Small Methods 3 (2018), 1800406.

[26] Y. Guo, S. Yao, L. Gao, A. Chen, M. Jiao, H. Cui, Z. Zhou, Boosting bifunctional electrocatalytic activity in S and N co-doped carbon nanosheets for high-efficiency Zn–air batteries, J. Mater. Chem. A 8 (2020) 4386–4395.

[27] H.B. Yang, S.-F. Hung, S. Liu, K. Yuan, S. Miao, L. Zhang, X. Huang, H.-Y. Wang, W. Cai, R. Chen, J. Gao, X. Yang, W. Chen, Y. Huang, H.M. Chen, C.M. Li, T. Zhang, B. Liu, Atomically dispersed Ni(i) as the active site for electrochemical CO2 reduction, Nat. Energy 3 (2018) 140–147.

[28] Y. Cheng, S. Zhao, H. Li, S. He, J.-P. Veder, B. Johannessen, J. Xiao, S. Lu, J. Pan, M.F. Chisholm, S.-Z. Yang, C. Liu, J.G. Chen, S.P. Jiang, Unsaturated edge-anchored Ni single atoms on porous microwave exfoliated graphene oxide for electrochemical CO2, Appl. Catal. B Environ. 243 (2019) 294–303.

[29] R. Daiyan, X. Zhu, Z. Tong, L. Gong, A. Razmjou, R.-S. Liu, Z. Xia, X. Lu, L. Dai, R. Amal, Transforming active sites in nickel–nitrogen–carbon catalysts for efficient electrochemical CO2 reduction to CO, Nano Energy 78 (2020), 105213.

[30] T. Zheng, K. Jiang, N. Ta, Y. Hu, J. Zeng, J. Liu, H. Wang, Hydrophobized SN38 to redox-hypersensitive nanorods for cancer therapy, Joule 3 (2019) 265–278.

[31] Z. Jiang, W. Sun, H. Shang, W. Chen, T. Sun, H. Li, J. Dong, J. Zhou, Z. Li, Y. Wang, R. Cao, R. Sarangi, Z. Yang, D. Wang, J. Zhang, Y. Li, Atomic interface effect of a single atom copper catalyst for enhanced oxygen reduction reactions, Energy Environ. Sci. 12 (2019) 3508–3514.

[32] J. Feng, H. Gao, L. Zheng, Z. Chen, S. Zeng, C. Jiang, H. Dong, L. Liu, S. Zhang, X. Zhang, A Mn-N3 single-atom catalyst embedded in graphitic carbon nitride for efficient CO2 electroreduction, Nat. Commun. 11 (2020) 4341.

[33] C.W. Li, M.W. Kanan, CO2 reduction at low overpotential on Cu electrodes resulting from the reduction of thick Cu2O films, J. Am. Chem. Soc. 134 (2012) 7231–7234.

[34] Y. Lu, H. Wang, P. Yu, Y. Yuan, R. Shahbazian-Yassar, Y. Sheng, S. Wu, W. Tu, G. Liu, M. Kraft, R. Xu, Isolated Ni single atoms in nitrogen doped ultrathin porous carbon templated from porous g-C3N4 for high-performance CO2 reduction, Nano Energy 77 (2020), 105158.

[35] S. Zhao, J. Yang, M. Han, X. Wang, Y. Lin, R. Yang, D. Xu, N. Shi, Q. Wang, M. Yang, Z. Dai, J. Bao, Synergistically enhanced oxygen reduction electrocatalysis by atomically dispersed and nanoscaled Co species in three-dimensional mesoporous Co, N-codoped carbon nanosheets network, Appl. Catal. B Environ. 260 (2020), 118207.

[36] P. Lu, Y. Yang, J. Yao, M. Wang, S. Dipazir, M. Yuan, J. Zhang, X. Wang, Z. Xie, G. Zhang, Facile synthesis of single-nickel-atomic dispersed N-doped carbon framework for efficient electrochemical CO2 reduction, Appl. Catal. B Environ. 241 (2019) 113–119.

[37] Z. Geng, Y. Cao, W. Chen, X. Kong, Y. Liu, T. Yao, Y. Lin, Regulating the coordination environment of Co single atoms for achieving efficient electrocatalytic activity in CO2 reduction, Appl. Catal. B Environ. 240 (2019) 234–240.

[38] Y. Lin, M. Zhou, X. Tai, H. Li, X. Han, J. Yu, Analytical transmission electron microscopy for emerging advanced materials, Matter 4 (2021) 2309–2339.

[39] W. Ma, H. Wan, L. Zhang, J.Y. Zheng, Z. Zhou, J. Energy Chem. (2021), https://doi.org/10.1016/j.jechem.2021.08.041.

[40] X. Li, W. Bi, M. Chen, Y. Sun, H. Ju, W. Yan, J. Zhu, X. Wu, W. Chu, C. Wu, Y. Xie, Exclusive Ni-N4 sites realize near-unity CO selectivity for electrochemical CO2 reduction, J. Am. Chem. Soc. 139 (2017) 14889–14892.

[41] J.K. Norskov, T. Bligaard, J. Rossmeisl, C.H. Christensen, Towards the computational design of solid catalysts, Nat. Chem. 1 (2009) 37–46.

[42] S. Yao, X. Zhang, A. Chen, Z. Zhang, M. Jiao, Z. Zhou, Algorithm screening to accelerate discovery of 2D metal-free electrocatalysts for hydrogen evolution reaction, J. Mater. Chem. A 7 (2019) 19290–19296.

[43] X. Zhang, A. Chen, L.T. Chen, Z. Zhou, 2D materials bridging experiments and computations for electro/photocatalysis, Adv. Energy Mater. 11 (2021), 2003841.